A Molecular Dynamics Protocol for Predicting EGFR Overactivation and Its Application to the Allosteric Mutations S768I, S768N, and D761N

Julian Behn[1,2], R. N. V. Krishna Deepak[1,3], Jiancheng Hu[4,5], and Hao Fan[1,4,6,7]

[1]Bioinformatics Institute (BII), Agency for Science, Technology and Research (A*STAR), Singapore 138671, Republic of Singapore.
[2]Yong Loo Lin School of Medicine, National University of Singapore, Singapore, Republic of Singapore.
[3]School of Arts and Sciences, Azim Premji University Bangalore, Bangalore, Republic of India.
[4]Cancer and Stem Cell Program, Duke-NUS Medical School, 8 College Road, Singapore 169857, Republic of Singapore.
[5]Division of Cellular and Molecular Research, National Cancer Centre Singapore, 11 Hospital Crescent, Singapore 169610, Republic of Singapore.
[6]Synthetic Biology Translational Research Program, Yong Loo Lin School of Medicine, National University of Singapore, Singapore 117597, Republic of Singapore.
[7]Department of Biochemistry, Yong Loo Lin School of Medicine, National University of Singapore, Singapore 117596, Republic of Singapore.

Abstract

Aberrant signaling due to mutations in the Epidermal Growth Factor Receptor (EGFR) kinase domain is implicated in various diseases, including cancer. However, the structural mechanisms underlying overactivation in many rare EGFR mutations remain poorly understood. Here, we benchmarked the CHARMM and AMBER force fields and compared simulations of asymmetric and symmetric dimers to establish a Molecular Dynamics (MD) protocol capable of revealing EGFR mutant actional modes using relatively short simulations. This protocol successfully reproduced the known mechanistic behavior of wild-type EGFR and two common mutations, L858R and T790M/L858R. We then applied it to three rare allosteric EGFR mutations: S768I, S768N, and D761N. Experimental studies have suggested that S768I and D761N are oncogenic, whereas S768N is likely a neutral mutation that does not significantly alter EGFR activity. Our simulations showed that S768I and S768N affect the orientation and stability of the catalytically important αC-helix allosterically, while D761N introduces a new hydrogen bonding network between the αC-helix and activation loop. These findings demonstrate how mutations induce distinct allosteric effects that alter EGFR dynamics and potentially contribute to overactivation. The benchmarking protocol established in this study provides a robust framework for investigating EGFR mutations and is readily applicable to additional variants.

Introduction

The Epidermal Growth Factor Receptor (EGFR) is a transmembrane tyrosine kinase receptor of significant clinical importance. Mutations in its intracellular kinase domain play a pivotal role in cancer development, particularly in Non-Small Cell Lung Cancer (NSCLC), the most prevalent form of lung cancer [1]. The prevalence of EGFR mutations in NSCLC varies demographically, ranging from 10 – 20% in Caucasians to 40 – 60% in Southeast Asians [2]. Targeted therapy using tyrosine kinase inhibitors (TKIs) has significantly improved treatment outcome for EGFR-related cancers [3]. However, treatment failure due to acquired or de novo resistance remains a major challenge in EGFR-targeted therapy [4]. Understanding the structural basis of oncogenic EGFR mutations is therefore essential for advancing therapeutic strategies.

The intracellular kinase domain of EGFR adopts a characteristic kinase fold, with an N-lobe and a C-lobe linked by a short hinge region (Figure 1a). This domain is highly dynamic and transitions between multiple conformations [5]. In the catalytically active conformation, the interlobal activation loop extends outward, allowing substrate access to the ATP pocket. Active kinases are also characterized by an inward-facing αC-helix. This αC-helix orientation facilitates the formation of the crucial K745 – E762 salt bridge, which aids in the coordination of the ATP – Mg^{2+} complex. Additionally, ATP binding is supported by the proper positioning of the highly conserved Asp-Phe-Gly (DFG) motif. In contrast, the ‘Src-like’ inactive conformation features a collapsed activation loop that obstructs the substrate-binding ATP pocket, an outward-facing αC-helix, and a disrupted K745 – E762 salt bridge. A second inactive EGFR conformation, the 'DFG-out' conformation, involves the DFG motif blocking ATP

binding. Most experimentally resolved EGFR structures, however, fall into either the active or Src-like inactive conformation, while in silico simulations have identified additional partially disordered states that may regulate EGFR activity [6-9]. In the absence of an activating ligand, wild-type EGFR predominantly favors the inactive state, and its conformational dynamics are further influenced by dimerization.

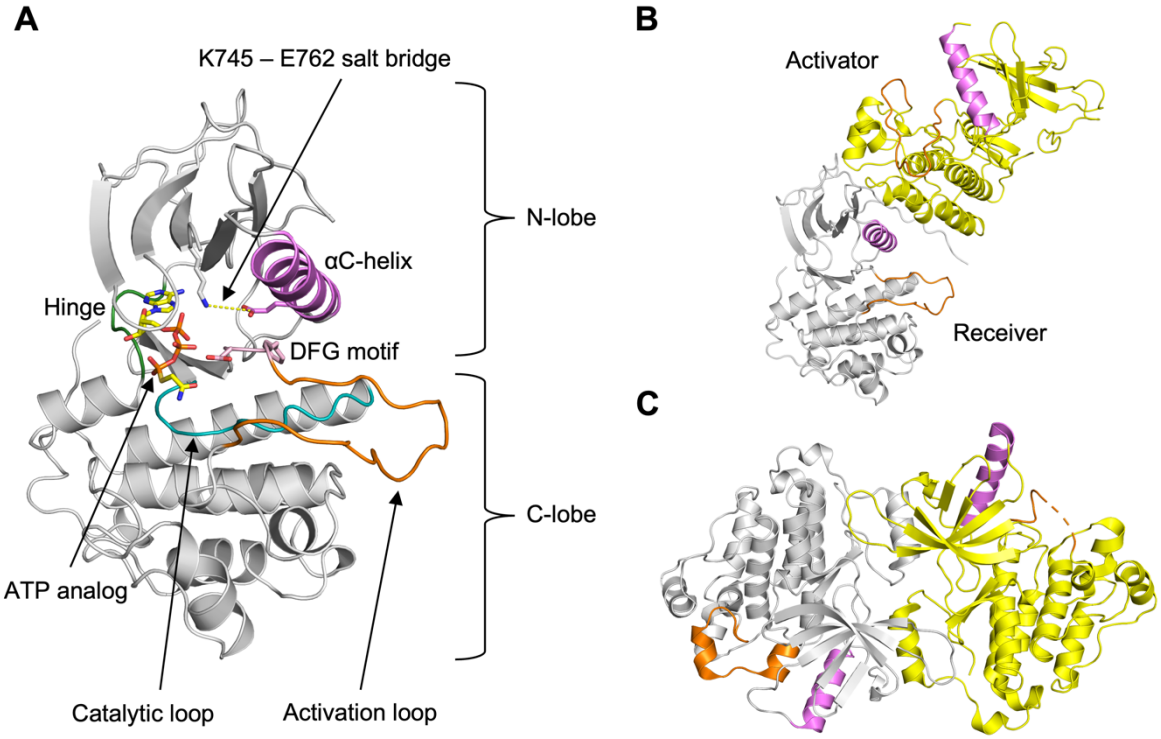

Figure 1. Structure of EGFR in monomeric and dimeric form.
(A) X-ray structure of the EGFR kinase domain in active conformation (PDB: 2GS6), with key structural features highlighted. (B) The kinase domain can form an asymmetric dimer, where both protomers adopt an active-like conformation. The receiver and activator chains are colored gray and yellow, respectively. (C) EGFR can also form a symmetric dimer, in which both chains adopt the Src-like inactive conformation (PDB: 6V66). In this arrangement, the activation loop is collapsed. The chains are colored gray and yellow, respectively. For better comparison, the αC-helices (violet) and activation loops (orange) are highlighted in both (B) and (C).

EGFR kinase domains form distinct intracellular dimer configurations that regulate activity. In the asymmetric dimer (Figure 1b), both chains adopt the active

conformation [10]. One chain, the activator, presses against the other, the receiver, locking the receiver's αC-helix in the active orientation. This dimerization mechanism is a crucial pre-requisite for the activation of wild-type EGFR under physiological conditions. Conversely, the symmetric dimer (Figure 1c) consists of two chains in the Src-like inactive conformation, stabilized by interactions between their C-terminal tails, and is believed to play a role in EGFR autoinhibition. Apart from the allosteric effects of dimerization on EGFR activity, mutations in the kinase domain can also modulate EGFR conformation and activity.

More than 500 different EGFR missense mutations have been recorded in the Catalogue of Somatic Mutations in Cancer (COSMIC) database. The exon 21 mutation L858R, along with exon 19 deletion mutations, is among the most frequent oncogenic driver mutations in EGFR-positive NSCLC [11]. Its role in causing overactivation and its response to targeted therapy have been extensively discussed in the literature. L858R is located at the beginning of the activation loop, adjacent to the DFG motif, and has been found to both stabilize the active conformation and disrupt the inactive conformation [6, 12-14]. Patients treated with TKIs for L858R-positive NSCLC frequently acquire a secondary resistance mutation, T790M, leading to the double mutation T790M/L858R. Although historically termed the ‘gatekeeper’ mutation, T790M/L858R confers drug resistance not through steric hindrance but likely by elevating ATP affinity [15].

Beyond these well-characterized mutations, hundreds of rare and ultra-rare EGFR mutations exist, many of which are not yet biochemically characterized, and for most, the structural mechanisms remain unknown. The rare exon 20 mutation S768I,

accounting for approximately 0.6 – 1% of EGFR mutations in NSCLC, has been well established as oncogenic in both experimental and clinical studies [16-18]. Located at the C-terminal end of the αC-helix and facing away from the binding site, S768I has been proposed by Shan et al. (identified as S744I in their study) to stabilize the active conformation through an allosteric mechanism [6]. In their simulations, they detected prolonged K745 – E762 salt bridge formation and increased αC-helix stability compared to the wild-type, and attributed these changes to enhanced hydrophobic packing between the mutated isoleucine residue in the αC-helix and the activation loop. However, their study did not quantify this increased hydrophobic packing. In contrast, an ultra-rare variant, S768N, located at the same position, has been experimentally suggested as a neutral mutation similar to the wild-type [19, 20]. The structural mechanism underlying S768N's non-activating nature, however, remains unknown.

Another αC-helix mutation, the exon 19 mutation D761N, has been identified in multiple tumor samples. It has been associated with increased EGFR activity and resistance to TKIs [20-22]. Like S768N, its structural mechanism remains unknown, though its location distal from the ATP-binding site suggests it alters EGFR activity through an allosteric mechanism.

Molecular Dynamics (MD) simulations are widely used to investigate the structural mechanisms of EGFR mutations by comparing the dynamics of mutants to wild-type EGFR. Previous EGFR simulation studies have employed diverse system configurations and protocols, varying in ATP inclusion, dimerization states, kinase domain conformation, simulation time, and force field parameters [1, 6-9, 12, 14, 23-

30]. To the best of our knowledge, no benchmarking study has been reported that establishes optimal simulation parameters specifically tailored for EGFR and its mutants. As a result, existing MD studies on EGFR may lack comparability unless the simulation protocols are clearly communicated and standardized.

Here, we conducted a benchmarking analysis to establish a standardized protocol for investigating EGFR mutants using MD simulations. We compared the CHARMM and AMBER force fields through simulations of wild-type, L858R, and the double mutant T790M/L858R as reference systems. We then applied this protocol to the allosteric mutations S768I, S768N, and D761N. Our simulations revealed distinct allosteric mechanisms by which these three mutations affect EGFR activation. Using our protocol, we could reproduce the previously reported increases in K745 – E762 salt bridge occupancy and αC-helix stability for the oncogenic S768I mutant. We also expanded upon previous findings by quantifying the proposed increase in hydrophobic interactions formed by S768I. In contrast, the hypothetically neutral mutation S768N increased local disorder by altering its hydrogen bonding pattern, forming less stable hydrogen bonds than wild-type, and exhibited reduced K745 – E762 salt bridge formation compared to S768I. Meanwhile, the oncogenic D761N mutation reshaped the hydrogen bonding network, introducing a novel and stable interaction pattern between the αC-helix and the activation loop. Together, our study demonstrated the utility of this MD protocol in elucidating the structural basis of allosteric EGFR overactivation. The critical roles of allosteric mechanisms in EGFR overactivation that are highlighted in this study could be considered in rational drug design and protein engineering efforts.

Results

Benchmarking of the Simulation Protocol

To establish an effective MD protocol for studying dynamic differences between wild-type and mutant EGFR, we compared two widely used force fields, CHARMM and AMBER. We simulated both the active-like and Src-like inactive conformations (hereafter referred to as ‘active’ and ‘inactive’ conformations, respectively). As discussed earlier, the active conformation is associated with the asymmetric dimer, whereas the inactive conformation can form a symmetric dimer. Accordingly, we simulated each conformation in its respective dimeric state. To assess the effect of ATP on EGFR dynamics, we simulated each dimer in both apo (no ligand present) and holo (ATP bound in the receiver monomer) conditions. Since the symmetric dimer lacks a defined receiver chain, ATP was placed arbitrarily in the first chain (chain ‘A’) as defined in the crystal structure assignment.

For benchmarking, we simulated wild-type (WT) EGFR, the oncogenic driver mutant L858R, and the common resistance double mutant T790M/L858R (TMLR). Each combination of force field, dimer type, apo/holo state, and mutation/wild-type status constituted a distinct simulation system. Each system was simulated using six independent replicas of 100 ns, amounting to 600 ns per system. With 24 systems in total, our benchmarking study comprised 14.4 μs of simulation time (Table S1).

CHARMM vs. AMBER: Simulating the Asymmetric Dimer

A well-established model to explain EGFR overactivation involves the stabilization of its active conformation [6, 12]. This active conformation is characterized by the formation of the catalytically important K745 – E762 salt bridge (Figure 2a). To

assess the stability of the active state, we measured the occupancy of this salt bridge in our simulations of the asymmetric dimer (Figure 2b).

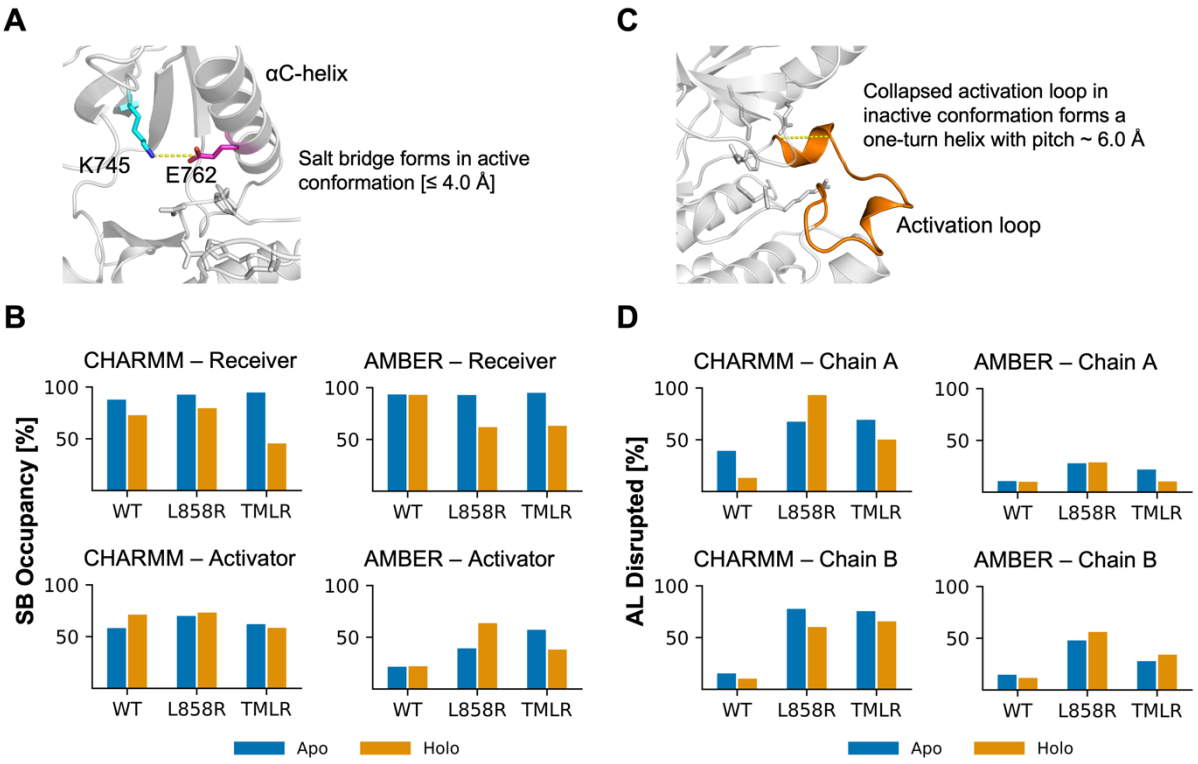

Figure 2. Benchmarking the CHARMM and AMBER force fields for reproducing known EGFR dynamics.
(A) In the active conformation, a salt bridge forms between residues K745 and E762. (B) Salt bridge occupancy using a cutoff of 4.0 Å in simulations of the asymmetric dimer. Values are shown for different force fields, chains, and the presence or absence of ATP. Note that data are presented only for the asymmetric dimer, as the K745 – E762 salt bridge did not form in simulations of the symmetric dimer. (C) In the Src-like inactive conformation, the activation loop is collapsed, forming a short, one-turn helix with a pitch of approximately 6.0 Å. (D) Disruption of the inactive activation loop conformation. The loop was considered disrupted if the helix pitch exceeded 7.0 Å. The percentage of simulation time during which the loop was disrupted is shown for different force fields, chains, and the presence or absence of ATP. Note that data are presented only for the symmetric dimer, as the one-turn helix was not observed in simulations of the asymmetric dimer. Abbreviations: SB = salt bridge, AL = activation loop.

In CHARMM simulations of the apo state, salt bridge occupancy in the receiver chain remained relatively consistent across variants (WT: 87.7%, L858R: 92.5%, TMLR: 94.7%). However, in the apo activator chain, L858R exhibited greater salt bridge

stability than WT and TMLR, with an occupancy more than 10 percentage points higher than WT (WT: 58.2%, L858R: 69.8%, TMLR: 61.9%).

AMBER apo simulations produced comparable results for the receiver chain (WT: 93.4%, L858R: 92.9%, TMLR: 94.9%), but salt bridge occupancies in the activator chain were generally lower than those observed in CHARMM and showed greater variation across mutants. Notably, TMLR exhibited the highest occupancy in the apo activator chain among WT and mutants, with an occupancy almost 40 percentage points higher than WT (WT: 21.3%, L858R: 39.1%, TMLR: 57.1%).

In CHARMM holo simulations of the asymmetric dimer, salt bridge occupancy in the receiver chain was slightly higher for L858R than in WT (WT: 72.7%, L858R: 79.5%), but was markedly reduced for TMLR (45.4%). Similarly, in the activator chain, occupancy showed a slight increase for L858R relative to WT (WT: 71.2%, L858R: 73.0%) but decreased by more than 10 percentage points for TMLR (58.4%).

In AMBER holo simulations, both L858R and TMLR exhibited lower salt bridge occupancy in the receiver chain compared to WT, with reductions of approximately 30 percentage points (WT: 93.0%, L858R: 61.8%, TMLR: 63.1%). In contrast, occupancy in the activator chain increased markedly for both mutants relative to WT (WT: 22.0%, L858R: 63.5%, TMLR: 38.0%).

Several key trends emerged from these simulations. Within each CHARMM simulation condition, L858R consistently exhibited higher salt bridge occupancy than WT, suggesting that it stabilizes the active EGFR conformation. In AMBER

simulations, this increase was observed only in the activator chain but not in the receiver chain. Additionally, the difference in salt bridge occupancy between WT and mutant activator chains was larger in AMBER simulations than in CHARMM, primarily due to the near absence of salt bridge formation in the WT activator chain in AMBER. Across both force fields, salt bridge occupancy in the receiver chain decreased upon ATP binding compared to apo conditions, likely due to the displacement of the E762 carboxylate group by ATP's phosphate moiety, causing K745 to interact with ATP rather than E762. Consequently, salt bridge occupancy in the holo receiver chain may not reliably indicate stabilization of the active conformation.

CHARMM vs. AMBER: Simulating the Symmetric Dimer

An alternative mechanism proposed for EGFR overactivation involves the destabilization of the inactive, symmetric dimer [12, 13]. In this model, mutations that reduce compatibility with the inactive conformation shift the conformational equilibrium toward the active state, potentially resulting in gain of function effects. The Src-like inactive conformation is characterized by a short, one-turn helix at the beginning of the activation loop, immediately following the DFG motif (Figure 2c). Consistent with previous studies, our simulations of the symmetric dimer showed that mutants disrupted this helix more frequently than WT. To quantify this effect, we measured helix disruption in the activation loop as a proxy for destabilization of the inactive state.

In CHARMM apo simulations of the symmetric dimer, activation loop disruption was observed 39.2% and 15.3% of the simulation time in chains A and B for WT,

respectively. In contrast, L858R exhibited a substantial increase in disruption: ~1.7-fold (67.4% of the time) and ~5.1-fold (77.6% of the time) relative to WT in chains A and B, respectively (Figure 2d). TMLR showed similar trends, with activation loop disruption occurring 69.1% and 75.4% of the time under CHARMM apo conditions in chains A and B, respectively.

AMBER apo simulations of the symmetric dimer also demonstrated increased activation loop disruption in mutants compared to WT. For WT, the activation loop disruption occurred 10.6% and 14.7% of the simulation time in apo chains A and B, respectively. In contrast, L858R showed a ~2.6-fold (27.8% of the time) and ~3.3-fold (47.7% of the time) increase in disruption relative to WT in chains A and B, respectively. TMLR exhibited a moderate increase, with disruptions of 21.8% and 27.7% under AMBER apo conditions in chain A and B, respectively.

In CHARMM holo simulations of the symmetric dimer, activation loop disruption increased sharply for L858R and TMLR compared to WT. While WT exhibited disruption in only 13.1% and 10.3% of the time in chains A and B, respectively, L858R showed a dramatic rise, with disruption occurring 93.0% and 60.1% of the time. TMLR also displayed increased disruption, at 50.1% and 65.6% in chains A and B, respectively.

In AMBER holo simulations, activation loop disruption in WT was observed 10.0% and 11.5% of the time in chain A and B, respectively. While L858R exhibited increased disruption in both chains (28.6% and 56.0% of the time), TMLR showed no

increase in chain A (10.3% of the time) but exhibited a moderate increase in chain B (34.0% of the time).

Overall, both CHARMM and AMBER simulations demonstrated that L858R and TMLR disrupt the inactive-like activation loop conformation more than WT. This effect was more pronounced in CHARMM, where the absolute increase in disruption was greater. While full transition to an extended activation loop conformation was not observed, the disruption of the activation loop helix suggests that L858R and TMLR destabilize the inactive state.

ATP exhibits greater binding stability in CHARMM simulations

To assess ATP behavior and interactions within the system, we analyzed its stability in our simulations. Surprisingly, ATP did not remain stably bound in the substrate binding pocket in AMBER simulations. Instead, the adenine moiety frequently exited the pocket and moved into the solvent in multiple simulations. This instability was reflected in higher average RMSD values for ATP in the active, asymmetric dimer in AMBER simulations compared to CHARMM (Figure 3 and Table 1). Higher RMSD values for ATP in AMBER were also observed for the inactive, symmetric dimer (Figure S1 and Table 1). Notably, comparison with a previous MD study on EGFR revealed that the authors using the AMBER force field also reported ATP interacting with residues outside the binding pocket [26].

Table 1. Average Root Mean Square Deviation (RMSD) of ATP (in Å) from simulations.

Dimer	Mutant	CHARMM	AMBER
Asymmetric	WT	2.7 ± 0.7	3.0 ± 1.4
	L858R	1.9 ± 0.5	2.7 ± 1.0
	TMLR	1.8 ± 0.5	4.8 ± 2.4
Symmetric	WT	1.3 ± 0.3	2.0 ± 0.6
	L858R	1.7 ± 0.5	2.0 ± 0.3
	TMLR	1.4 ± 0.4	1.9 ± 0.4

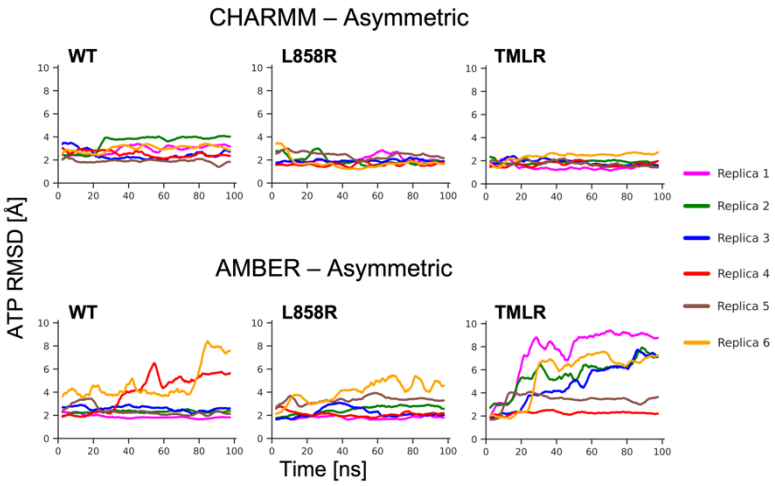

Figure 3. ATP stability in the CHARMM and AMBER force fields.
Root Mean Square Deviation (RMSD) of ATP (in Å) in simulations of the asymmetric dimer for WT, L858R, and TMLR. Line plots show rolling averages over 5 ns for each independent replica. See also Figure S1 for ATP RMSD in symmetric dimer simulations.

Evaluation of the benchmarking study

We then evaluated which protocol to use for simulating additional variants. While both force fields produced results that generally aligned with existing findings for WT and mutants, we opted to continue using only the CHARMM force field for three main reasons. First, CHARMM more consistently captured the expected increase in K745 – E762 salt bridge stability of L858R relative to WT in asymmetric dimer simulations (Figure 2b). In contrast, AMBER showed a more pronounced increase in salt bridge occupancy in the activator chain for L858R relative to WT compared to CHARMM,

but showed no increase in the receiver chain. Second, CHARMM better captured the destabilization of the inactive conformation by the cancer mutants (Figure 2d). In CHARMM simulations, L858R and TMLR caused a more pronounced disruption of the inactive activation loop conformation, with the majority of CHARMM systems showing markedly increased disruption relative to WT. Third, ATP binding was more stable in CHARMM. In AMBER, ATP partially dissociated from the binding site in several simulations (Figure 3), whereas in CHARMM, ATP remained relatively stably bound throughout. We therefore concluded that using the CHARMM force field alone is sufficient to capture mutational overactivation.

We then applied this MD protocol to study the rare mutations S768I, S768N, and D761N. Each mutant was simulated in asymmetric and symmetric dimeric forms under apo and holo conditions with the CHARMM force field, using five independent 100 ns replicas per system, totaling 500 ns per system and 2 μs per mutant (Table S2).

S768I exhibits increased hydrophobic packing between αC-helix and activation loop

The oncogenic mutation S768I has been reported to stabilize the αC-helix and enhance K745 – E762 salt bridge formation compared to the wild-type. This stabilization has been attributed to increased hydrophobic packing introduced by the mutation. To assess whether our simulations reproduced these findings, we analyzed salt bridge formation, secondary structure stability, and the number of hydrophobic contacts formed by residue 768. Additionally, we investigated whether S768I disrupts the inactive conformation.

As expected, apo simulations of the asymmetric dimer confirmed that the K745 – E762 salt bridge is more stable in S768I than in WT (Figure 4a): the salt bridge forms 96.6% of the time in the receiver chain of S768I (WT: 87.7%, for comparison: L858R: 92.5%) and 78.4% of the time in the activator chain, which is more than 20 percentage points higher than WT (WT: 58.2%, L858R: 69.8%). In the holo simulations of the asymmetric dimer, S768I exhibited decreased salt bridge formation (51.9%) relative to WT in the receiver chain (WT: 72.7%, L858R: 79.5%), but increased formation (78.3%) in the activator chain (WT: 71.2%, L858R: 73.0%). To determine whether the mutated residue directly interacts with the salt bridge residues, we measured its proximity to key catalytic sites. In all simulations, the sidechain heavy atoms of both WT and mutant residue 768 remained beyond 7 Å from the side chains of K745 and E762, 10 Å from the sidechain of the catalytic aspartate D855 of the DFG motif, and 10 Å from any ATP heavy atom. Therefore, residue S768 does not directly interact with ATP or catalytically relevant residues, suggesting an allosteric mechanism for the increase in salt bridge formation.

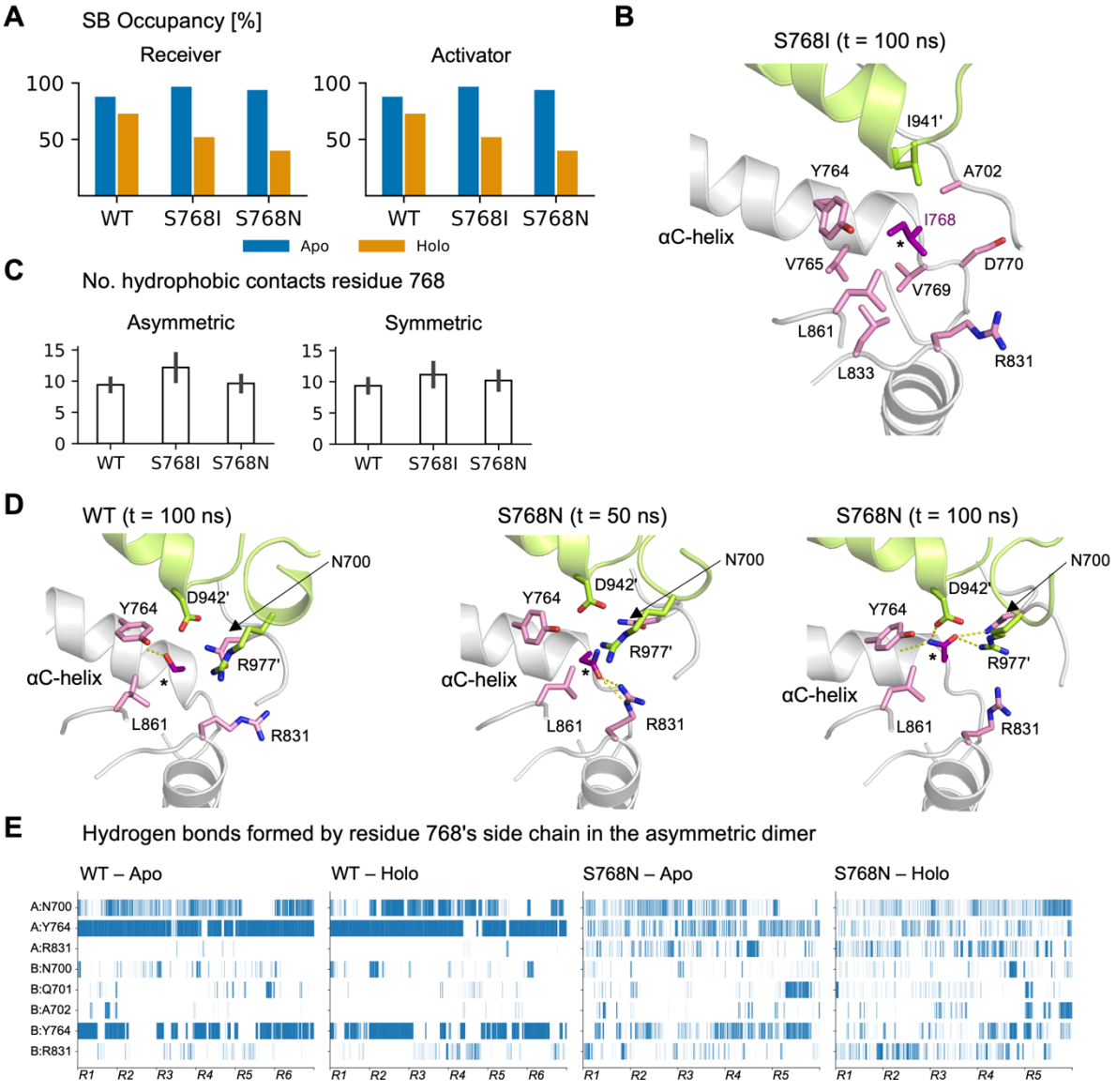

Figure 4. Allosteric regulation in the mutant pair S768I and S768N. (A) Comparison of salt bridge occupancy in the asymmetric dimer among WT, S768I, and S768N, analogous to Figure 2b. (B) Snapshot of the S768I mutant in the asymmetric dimer conformation after 100 ns of simulation time. The mutant residue I768 and surrounding residues form a hydrophobic network. The receiver and activator chains are highlighted in light gray and green, respectively. I768 is highlighted in purple and labeled with an asterisk. Other residues of the receiver chain are shown in pink stick representation, while residues of the activator chain are depicted in green stick representation. (C) Average number of hydrophobic contacts between residue S/I/N768 and its neighboring residues, calculated across both Apo and Holo systems. Error bars show standard deviation. (D) Snapshots of WT and the S768N mutant at different simulation times. Hydrogen bonds involving the sidechain of residue 768 are shown as yellow dashed lines. The receiver and activator chains are highlighted in light gray and green, respectively. Residue 768 is highlighted in purple and labeled with an asterisk. Other residues of the receiver chain are shown in pink stick representation, while residues of the activator chain are depicted in green stick representation. (E) Hydrogen bond existence map illustrating interactions between the sidechain of residue 768 and its surrounding environment over time.

Each residue is labeled by its chain: A = receiver chain, B = activator chain. Only hydrogen bonds with a frequency of 5% or higher in at least one system are shown. Data from all replicas are combined for each system. Abbreviations: SB = salt bridge, Rep = Replica.

To investigate the reported stabilization of the active conformation of the αC-helix, we analyzed its secondary structure stability using the DSSP method. Consistent with previous findings, S768I exhibited greater αC-helix stability in the asymmetric dimer compared to WT, with a higher average number of residues assigned as 'helical' in both apo and holo simulations. In the apo state, this increase was observed in both the receiver (S768I: 15.4 ± 1.1, WT: 14.9 ± 1.2) and activator (S768I: 15.4 ± 1.1, WT: 14.8 ± 1.6) chains. A similar trend was seen in holo simulations, with S768I maintaining a higher number of helical residues in both the receiver (S768I: 15.7 ± 0.8, WT: 14.7 ± 1.4) and activator (S768I: 14.9 ± 1.5, WT: 14.5 ± 1.5) chains.

To quantify the reported increase in hydrophobic packing, we measured hydrophobic contacts between residue 768 and its neighboring residues (Figure 4b,c). Supporting previous claims, S768I exhibited approximately 30% more hydrophobic interactions than WT. This increase was observed in all conditions: apo receiver chain (WT: 9.4 ± 0.9, S768I: 11.8 ± 2.0), apo activator chain (WT: 9.4 ± 1.2, S768I: 12.3 ± 2.3), holo receiver chain (WT: 9.5 ± 1.0, S768I: 12.1 ± 2.0), and holo activator chain (WT: 9.2 ± 1.0, S768I: 12.5 ± 2.3).

We also analyzed the disruption of the short one-turn helix in the collapsed activation loop in simulations of the inactive, symmetric dimer. Compared to WT, S768I exhibited reduced activation loop disruption in apo chain A (WT: 39.2%, S768I:

27.8%) but increased disruption in apo chain B (WT: 15.3%, S768I: 38.4%), holo chain A (WT: 13.1%, S768I: 16.5%), and holo chain B (WT: 10.3%, S768I: 27.6%). However, even in systems where S768I increased disruption of the inactive state, the effect was less pronounced than in L858R or TMLR (Figure 2d and Table S3), suggesting that S768I does not strongly destabilize the inactive state.

In summary, our simulations of the asymmetric dimer showed that S768I increases salt bridge formation under apo conditions, enhances αC-helix stability, and strengthens hydrophobic packing. Notably, the increase in salt bridge formation was greater than that of the strongly oncogenic L858R under all conditions except for the receiver chain in holo simulations, where salt bridge stability – as mentioned before – may not be an indicative measure of EGFR overactivation. The increase in hydrophobic interactions between the mutated residue 768 and hydrophobic residues from both the αC-helix and activation loop (Figures 4b,c) likely contributes to the observed stabilization of the αC-helix. Given that E762, one of the two residues involved in the catalytic salt bridge, is part of the αC-helix, this stabilization may play a role in reinforcing the salt bridge. Since S768I did not induce as strong a disruption of the inactive state as L858R and TMLR, we hypothesize that its oncogenic effects primarily stem from stabilizing the active state rather than destabilizing the inactive conformation.

S768N increases local disorder through formation of a dynamic hydrogen bonding network

To investigate the structural basis for the presumed non-activating behavior of the S768N mutant, we performed the same analyses as for the oncogenic S768I mutant.

As expected, S768N exhibited reduced salt bridge formation and weaker hydrophobic packing compared to S768I (Figures 4a,c) in the asymmetric dimer. Additionally, αC-helix stability in S768N was either lower or comparable to WT. In the apo state, this reduction was observed in both the receiver (S768N: 14.2 ± 1.2, WT: 14.9 ± 1.2) and activator (S768N: 14.5 ± 1.5, WT: 14.8 ± 1.6) chains. A similar trend was seen in holo simulations, where S768N maintained comparable or reduced numbers of helical residues in both the receiver (S768N: 14.7 ± 1.5, WT: 14.7 ± 1.4) and activator (S768N: 14.3 ± 2.0, WT: 14.5 ± 1.5) chains.

We also analyzed the disruption of the collapsed activation loop in the symmetric dimer. Compared to WT and S768I, S768N exhibited increased activation loop disruption. However, this effect was less pronounced than in L858R or TMLR (Table S3). These findings suggest that S768N is unlikely to confer a gain of function, supporting its classification as a neutral mutation. To further explore why the structural changes caused by S768N were likely insufficient to drive overactivation, we investigated their impacts on the local hydrogen bonding network.

We hypothesized that the asparagine substitution in S768N might alter hydrogen bonding patterns, thereby affecting the stability of the active conformation. To test this, we analyzed hydrogen bonding interactions involving the serine side chain in WT and the asparagine side chain in S768N (Figure 4d). Interestingly, while S768N is theoretically capable of forming more hydrogen bonds – at times forming up to five simultaneously in our simulations – the average number of hydrogen bonds observed across simulation snapshots was equal to or lower than in WT. In apo simulations of the asymmetric dimer, the WT serine side chain formed an average of 1.4 ± 0.5 and 0.8 ± 0.7 hydrogen bonds in the receiver chain and the activator

chains, respectively. In contrast, the S768N side chain formed 0.9 ± 0.7 and 0.8 ± 0.9 hydrogen bonds in the receiver and activator chains, respectively. Similar trends were observed in holo simulations, where WT formed 1.4 ± 0.5 and 0.8 ± 0.6 hydrogen bonds, while S768N formed 0.8 ± 0.7 and 0.9 ± 0.9 hydrogen bonds in the receiver and activator chains, respectively.

Next, we examined the hydrogen bonding partners of residue 768 in our asymmetric dimer simulations (Figure 4e). In WT, hydrogen bonds were primarily formed with the backbone carbonyl oxygen of the αC-helix residue Y764 and, less frequently, with the side chain of N700 in the N-terminal tail. In contrast, the side chain of S768N exhibited greater flexibility, frequently switching hydrogen bonding partners between N700, Y764, and R831 (located in the αE-helix of the C-lobe), with occasional interactions with Q701 and A702. We propose that this increased flexibility, which resulted in an overall reduction in hydrogen bond stability due to numerous short-lived interactions, contributes to greater disorder in the αC-helix and may explain the presumed non-activating behavior of S768N. Interestingly, in the inactive, symmetric dimer, S768N formed slightly more hydrogen bonds than WT (Table S4), potentially suggesting a modest stabilizing effect on the inactive state.

D761N forms a new hydrogen bonding pattern between the αC-helix and activation loop

We also simulated the oncogenic exon 19 mutation D761N, located near the center of the αC-helix. When measuring salt bridge occupancy in the apo asymmetric dimer, we found that D761N exhibited the highest occupancy among all simulated mutants in the receiver chain, increasing by almost 10 percentage points compared to WT

(from 87.7% to 97.5%, Figure 5a). In contrast, salt bridge occupancy decreased in the activator chain (WT: 58.2%, D761N: 49.3%). This suggests that D761N primarily stabilizes the active conformation in the receiver chain but not in the activator chain. Additionally, D761N did not increase activation loop disruption relative to WT in the inactive, symmetric dimer (Table S3). Therefore, similar to S768I, our simulations suggest that D761N primarily stabilizes the active state rather than destabilizing the inactive state.

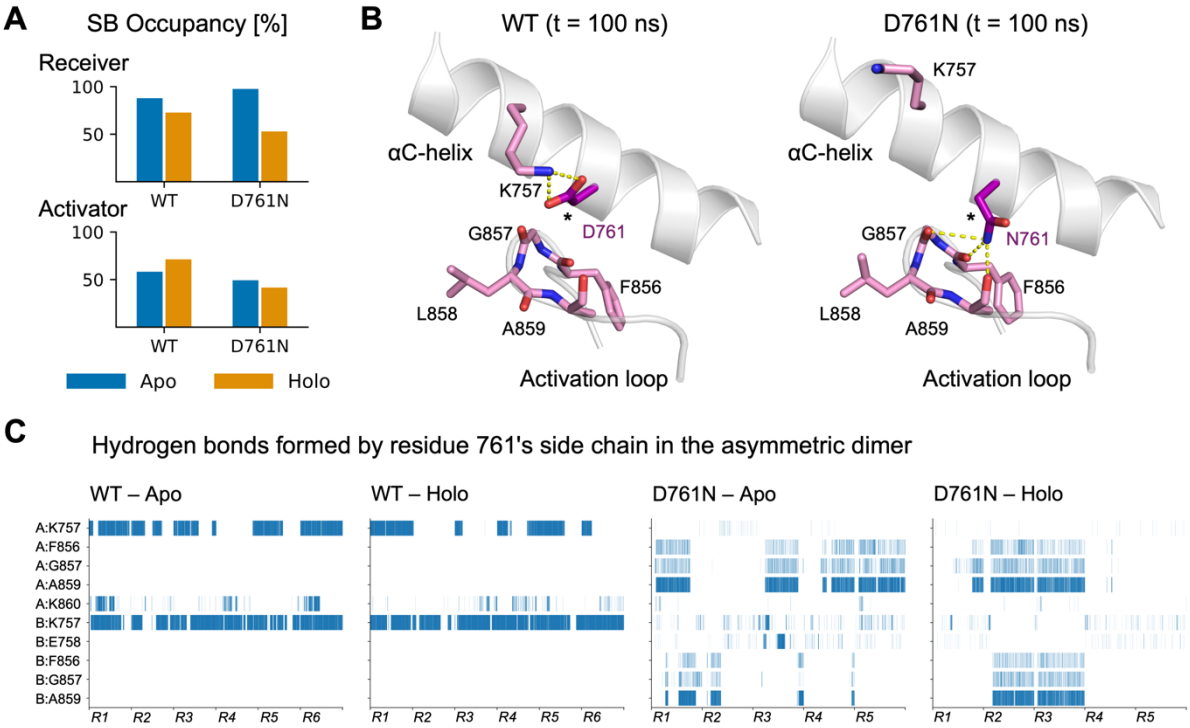

Figure 5. The D761N mutation forms a new hydrogen bonding pattern between the αC-helix and the activation loop.
(A) Comparison of salt bridge occupancy in the asymmetric dimer among WT and D761N, analogous to Figure 2b. (B) Snapshots of WT and the D761N mutant after 100 ns of simulation time each. Hydrogen bonds involving the sidechain of residue 761 are shown as yellow dashed lines. The snapshots display the receiver chain, with residue 761 highlighted in purple and marked with an asterisk. For residues 856-859, the backbone atoms are also shown. (C) Hydrogen bond existence map illustrating interactions between the sidechain of residue 761 and its surrounding environment over time. Each residue is labeled by its chain: A = receiver chain, B = activator chain. Only hydrogen bonds with a frequency of 5% or higher in at least one system are shown. Data from all replicas are combined for each system. Abbreviations: SB = salt bridge, R = Replica.

To further explore the structural effects of D761N, we examined the local hydrogen bonding network around the mutant site (Figure 5b). Interestingly, D761N formed a stable alternative hydrogen bonding network distinct from that of WT. In WT, the aspartate side chain of D761 primarily formed a salt bridge with the more N-terminal lysine K757. In contrast, the mutated asparagine side chain in the D761N mutant frequently engaged in hydrogen bonds with the backbones of residues F856, G857, and A859 (Figure 5c). Notably, F856 and G857 belong to the DFG motif, and all three residues are part of the activation loop. In the apo state, these hydrogens bonds formed more frequently in the receiver chain than in the activator chain, aligning with the high salt bridge stability observed for the apo receiver chain. Conversely, under holo conditions, the hydrogen bond formation was more balanced between the receiver and activator chains, which also corresponded to the similar salt bridge occupancy between the holo receiver and activator chains (Figure 5a). These findings suggest that D761N stabilizes a novel hydrogen bonding pattern between the αC-helix and the activation loop, potentially promoting the active conformation allosterically and contributing to oncogenicity.

Discussion

A novel protocol to study EGFR overactivation

Long-timescale unbiased MD simulations have been widely employed to study EGFR conformational transitions, with some studies extending into the hundreds of microseconds of simulation time [6, 7]. Others have used enhanced sampling methods to explore a broader conformational space [8, 12]. Here, we presented a protocol that utilizes sets of 100 ns unbiased simulations to compare the dynamics of wild-type EGFR and its mutants. This timescale is sufficient to observe disruptions in

the active EGFR state [6]. Although the Src-like inactive state is relatively stable – having been simulated for up to 100 μs in previous studies – our analysis of activation loop stability in the inactive, symmetric dimer captured local disruptions well within our 100 ns replicas. To ensure reproducibility in system preparation and simulation setup, we used the well-established CHARMM-GUI web interface (see Methods). This approach standardizes the simulation workflow, particularly for extending studies to additional EGFR variants. Furthermore, our analysis steps are easily repeatable and can serve as a blueprint for studying other EGFR mutations or even other kinase family members.

By simulating both the active, asymmetric dimer and the inactive, symmetric dimer, our protocol enables identification of whether a mutation primarily affects the active state, the inactive state, or both. This distinction has practical implications for drug design, as different classes of tyrosine kinase inhibitors (TKIs) target specific EGFR conformations [31]. Notably, Type I TKIs bind to the active state, while Type I.5 TKIs preferentially target the Src-like inactive state. Understanding the mechanism of overactivation, as revealed by our protocol, could help guide the selection of therapeutic strategies by identifying which conformational state to target.

Applicability to further variants

We aimed to establish criteria to determine whether a mutation is likely oncogenic based on our protocol. Our results suggest that apo simulations alone are sufficient to distinguish between oncogenic and neutral mutants. Across our CHARMM apo simulations, we observed that all oncogenic mutations in this study – except TMLR – increased salt bridge occupancy by at least 10 percentage points in at least one

chain of the apo asymmetric dimer, compared to WT (which exhibited 87.7% and 58.2% occupancy in the receiver and activator chains, respectively). Meanwhile, TMLR and L858R were the only oncogenic mutants that consistently exhibited high disruption of the inactive state. Under apo conditions, both mutations disrupted the inactive conformation in more than 60% of the simulation time for both chains – a threshold that no other mutant exceeded in apo simulations. Based on these observations, a mutation is likely oncogenic if it meets at least one of the following three criteria in apo simulations: (i) salt bridge occupancy of 97% or higher in the receiver chain of the asymmetric dimer, (ii) salt bridge occupancy of 68% or higher in the activator chain of the asymmetric dimer, (iii) disruption of the inactive state in at least 60% of the simulation time for both chains in the symmetric dimer. We suspect that the likelihood of oncogenicity increases if multiple criteria are met. Additionally, if ambiguity remains, holo simulations may provide further insights.

Conclusion

The EGFR kinase domain exhibits a vast mutational landscape, with nearly 1,000 recorded somatic mutations cataloged in COSMIC, including over 500 missense mutations. Despite this diversity, only a small fraction of these mutants has been biochemically characterized, and even fewer have been studied at the structural level. Our MD protocol successfully captured the differences between wild-type EGFR and the oncogenic and neutral mutations studied here. For the frequent oncogenic mutations L858R and T790M/L858R, our simulations demonstrated both stabilization of the active state and disruption of the inactive state, consistent with their known oncogenic mechanisms. In contrast, the rare oncogenic mutations S768I and D761N stabilized the active conformation, with our simulations suggesting

allosteric mechanisms as the underlying cause – either through increased hydrophobic packing around the αC-helix (S768I) or the formation of a new hydrogen bonding network between the αC-helix and activation loop (D761N). Meanwhile, the neutral mutation S768N failed to stabilize the active conformation, likely due to an unstable and overly flexible hydrogen bonding network introduced by the mutation. Importantly, our study demonstrates that even relatively short 100 ns simulations – which can typically be completed within two days on modern computational hardware – are sufficient to capture key mutational effects on EGFR overactivation. These results highlight the potential of MD simulations for rapidly screening EGFR mutations and gaining insights into their structural and functional consequences.

Materials and Methods

Structural modeling

The initial structures for the simulation of EGFR kinase domain dimers were generated using the homology modeling software MODELLER (version 10.4) [32], based on a template structure in the active conformation (PDB:2GS6) for the asymmetric dimer and a template structure in the inactive conformation (PDB:6V66) for the symmetric dimer. ATP + Mg^{2+} were placed in the ATP-binding pockets of the template structures to obtain ATP-bound templates. The canonical EGFR UniProt sequence (AC:P00533), from residue 697 to 1022, was selected as the target sequence for the wild-type. Mutations were introduced into the wild-type sequence at the appropriate location to generate the target sequences for the mutants. For each target sequence, 2000 models were generated for both the asymmetric and symmetric ATP-dimer complexes, and the best model from each set was selected based on the DOPE score [33]. The quality of the generated models was evaluated

using MolProbity [34]. Apo structures were obtained by removing ATP + Mg^{2+} from the models.

Molecular Dynamics (MD) simulations

All simulations were performed with GROMACS (versions 2021.5 and 2022.1) [35], using the CHARMM36m force field [36] for CHARMM-based simulations and the AMBER ff19SB force field [37] for AMBER-based simulations. The input files for the simulations were generated with the CHARMM-GUI web interface (https://www.charmm-gui.org) [38-41]. The N-terminus ($-NH_2$) and C-terminus (-COOH) of EGFR were capped by acetylation and amidation, respectively. Histidine residues were treated as δ-nitrogen protonated, except for histidine 835, which was treated as ε-nitrogen protonated. In the holo simulations, the ATP molecule was assigned a 4-fold negative charge. Each EGFR dimer was solvated in a rectangular box with an edge distance of 10.0 Å from the solute, and the total charge of each system was neutralized by the addition of Na^+ and Cl^- ions to a final concentration of 0.15 M. Systems were energy-minimized using the steepest descent algorithm and then equilibrated for 125 ps under NVT conditions at 303.15 K. Production runs under NPT conditions were subsequently carried out in 100 ns chunks ('replicas') with randomly initialized velocities. Each system was simulated with five replicas for S768I, S768N, and D761N, and six replicas for WT, L858R, and T790M/L858R. The total cumulative simulation time per system is described in the Results section (see also Tables S1 and S2 in the Supplementary Material).

Data analysis and visualization

Averages are presented as mean ± standard deviation. Simulation trajectories were analyzed using built-in tools from GROMACS and the Python library MDTraj [42]. Activation loop disruption was defined as occurring when the one-turn helix pitch exceeded a cutoff of 7.0 Å. For RMSD calculations, simulation snapshots were superposed based on the backbone atoms of helices in the rigid C-lobe (residues 812 – 831, 892 – 908, 941 – 950, 961 – 972). Only heavy atoms were considered for the RMSD calculations. Protein structures were visualized using the PyMOL Molecular Graphics System, Version 3.0.2 Schrödinger, LLC.

Acknowledgements

The computational work for this article was partially performed on resources of the National Supercomputing Centre (NSCC), Singapore (https://www.nscc.sg). JB is supported by the Singapore International Graduate Award (SINGA), A*STAR, Singapore. HF is supported by funding from Bioinformatics Institute, A*STAR, Singapore.

Appendix A. Supplementary Material

References

[1] Yoshizawa T, Uchibori K, Araki M, Matsumoto S, Ma B, Kanada R, et al. Microsecond-timescale MD simulation of EGFR minor mutation predicts the structural flexibility of EGFR kinase core that reflects EGFR inhibitor sensitivity. NPJ Precis Oncol. 2021;5:32.

[2] Hsu WH, Yang JC, Mok TS, Loong HH. Overview of current systemic management of EGFR-mutant NSCLC. Ann Oncol. 2018;29:i3-i9.

[3] Huang L, Jiang S, Shi Y. Tyrosine kinase inhibitors for solid tumors in the past 20 years (2001-2020). J Hematol Oncol. 2020;13:143.

[4] Zhang T, Wan B, Zhao Y, Li C, Liu H, Lv T, et al. Treatment of uncommon EGFR mutations in non-small cell lung cancer: new evidence and treatment. Transl Lung Cancer Res. 2019;8:302-16.
[5] Modi V, Dunbrack RL, Jr. Defining a new nomenclature for the structures of active and inactive kinases. Proc Natl Acad Sci U S A. 2019;116:6818-27.
[6] Shan Y, Eastwood MP, Zhang X, Kim ET, Arkhipov A, Dror RO, et al. Oncogenic mutations counteract intrinsic disorder in the EGFR kinase and promote receptor dimerization. Cell. 2012;149:860-70.
[7] Shan Y, Arkhipov A, Kim ET, Pan AC, Shaw DE. Transitions to catalytically inactive conformations in EGFR kinase. Proc Natl Acad Sci U S A. 2013;110:7270-5.
[8] Li Y, Li X, Ma W, Dong Z. Conformational Transition Pathways of Epidermal Growth Factor Receptor Kinase Domain from Multiple Molecular Dynamics Simulations and Bayesian Clustering. J Chem Theory Comput. 2014;10:3503-11.
[9] Galdadas I, Carlino L, Ward RA, Hughes SJ, Haider S, Gervasio FL. Structural basis of the effect of activating mutations on the EGF receptor. Elife. 2021;10.
[10] Zhang X, Gureasko J, Shen K, Cole PA, Kuriyan J. An allosteric mechanism for activation of the kinase domain of epidermal growth factor receptor. Cell. 2006;125:1137-49.
[11] Gazdar AF. Activating and resistance mutations of EGFR in non-small-cell lung cancer: role in clinical response to EGFR tyrosine kinase inhibitors. Oncogene. 2009;28 Suppl 1:S24-31.
[12] Sutto L, Gervasio FL. Effects of oncogenic mutations on the conformational free-energy landscape of EGFR kinase. Proc Natl Acad Sci U S A. 2013;110:10616-21.
[13] Yun CH, Boggon TJ, Li Y, Woo MS, Greulich H, Meyerson M, et al. Structures of lung cancer-derived EGFR mutants and inhibitor complexes: mechanism of activation and insights into differential inhibitor sensitivity. Cancer Cell. 2007;11:217-27.
[14] Wan S, Coveney PV. Molecular dynamics simulation reveals structural and thermodynamic features of kinase activation by cancer mutations within the epidermal growth factor receptor. J Comput Chem. 2011;32:2843-52.
[15] Yun CH, Mengwasser KE, Toms AV, Woo MS, Greulich H, Wong KK, et al. The T790M mutation in EGFR kinase causes drug resistance by increasing the affinity for ATP. Proc Natl Acad Sci U S A. 2008;105:2070-5.
[16] Banno E, Togashi Y, Nakamura Y, Chiba M, Kobayashi Y, Hayashi H, et al. Sensitivities to various epidermal growth factor receptor-tyrosine kinase inhibitors of uncommon epidermal growth factor receptor mutations L861Q and S768I: What is the optimal epidermal growth factor receptor-tyrosine kinase inhibitor? Cancer Sci. 2016;107:1134-40.
[17] Leventakos K, Kipp BR, Rumilla KM, Winters JL, Yi ES, Mansfield AS. S768I Mutation in EGFR in Patients with Lung Cancer. J Thorac Oncol. 2016;11:1798-801.
[18] Harrison PT, Vyse S, Huang PH. Rare epidermal growth factor receptor (EGFR) mutations in non-small cell lung cancer. Semin Cancer Biol. 2020;61:167-79.
[19] Harada T, Lopez-Chavez A, Xi L, Raffeld M, Wang Y, Giaccone G. Characterization of epidermal growth factor receptor mutations in non-small-cell lung cancer patients of African-American ancestry. Oncogene. 2011;30:1744-52.
[20] Ng PK, Li J, Jeong KJ, Shao S, Chen H, Tsang YH, et al. Systematic Functional Annotation of Somatic Mutations in Cancer. Cancer Cell. 2018;33:450-62 e10.
[21] Kancha RK, von Bubnoff N, Peschel C, Duyster J. Functional analysis of epidermal growth factor receptor (EGFR) mutations and potential implications for EGFR targeted therapy. Clin Cancer Res. 2009;15:460-7.

[22] Ma L, Li H, Wang D, Hu Y, Yu M, Zhang Q, et al. Dynamic cfDNA Analysis by NGS in EGFR T790M-Positive Advanced NSCLC Patients Failed to the First-Generation EGFR-TKIs. Front Oncol. 2021;11:643199.
[23] Shih AJ, Telesco SE, Choi SH, Lemmon MA, Radhakrishnan R. Molecular dynamics analysis of conserved hydrophobic and hydrophilic bond-interaction networks in ErbB family kinases. Biochem J. 2011;436:241-51.
[24] Songtawee N, Bevan DR, Choowongkomon K. Molecular dynamics of the asymmetric dimers of EGFR: simulations on the active and inactive conformations of the kinase domain. J Mol Graph Model. 2015;58:16-29.
[25] Park J, McDonald JJ, Petter RC, Houk KN. Molecular Dynamics Analysis of Binding of Kinase Inhibitors to WT EGFR and the T790M Mutant. J Chem Theory Comput. 2016;12:2066-78.
[26] Saldana-Rivera L, Bello M, Mendez-Luna D. Structural insight into the binding mechanism of ATP to EGFR and L858R, and T790M and L858R/T790 mutants. J Biomol Struct Dyn. 2019;37:4671-84.
[27] Kannan S, Venkatachalam G, Lim HH, Surana U, Verma C. Conformational landscape of the epidermal growth factor receptor kinase reveals a mutant specific allosteric pocket. Chem Sci. 2018;9:5212-22.
[28] Ikemura S, Yasuda H, Matsumoto S, Kamada M, Hamamoto J, Masuzawa K, et al. Molecular dynamics simulation-guided drug sensitivity prediction for lung cancer with rare EGFR mutations. Proc Natl Acad Sci U S A. 2019;116:10025-30.
[29] Tamirat MZ, Koivu M, Elenius K, Johnson MS. Structural characterization of EGFR exon 19 deletion mutation using molecular dynamics simulation. PLoS One. 2019;14:e0222814.
[30] Laudadio E, Mobbili G, Sorci L, Galeazzi R, Minnelli C. Mechanistic insight toward EGFR activation induced by ATP: role of mutations and water in ATP binding patterns. J Biomol Struct Dyn. 2023;41:6492-501.
[31] Roskoski R, Jr. Classification of small molecule protein kinase inhibitors based upon the structures of their drug-enzyme complexes. Pharmacol Res. 2016;103:26-48.
[32] Sali A, Blundell TL. Comparative protein modelling by satisfaction of spatial restraints. J Mol Biol. 1993;234:779-815.
[33] Shen MY, Sali A. Statistical potential for assessment and prediction of protein structures. Protein Sci. 2006;15:2507-24.
[34] Williams CJ, Headd JJ, Moriarty NW, Prisant MG, Videau LL, Deis LN, et al. MolProbity: More and better reference data for improved all-atom structure validation. Protein Sci. 2018;27:293-315.
[35] Abraham MJ, Murtola T, Schulz R, Páll S, Smith JC, Hess B, et al. GROMACS: High performance molecular simulations through multi-level parallelism from laptops to supercomputers. SoftwareX. 2015;1-2:19-25.
[36] Huang J, Rauscher S, Nawrocki G, Ran T, Feig M, de Groot BL, et al. CHARMM36m: an improved force field for folded and intrinsically disordered proteins. Nat Methods. 2017;14:71-3.
[37] Tian C, Kasavajhala K, Belfon KAA, Raguette L, Huang H, Migues AN, et al. ff19SB: Amino-Acid-Specific Protein Backbone Parameters Trained against Quantum Mechanics Energy Surfaces in Solution. J Chem Theory Comput. 2020;16:528-52.
[38] Jo S, Kim T, Iyer VG, Im W. CHARMM-GUI: a web-based graphical user interface for CHARMM. J Comput Chem. 2008;29:1859-65.

[39] Brooks BR, Brooks CL, 3rd, Mackerell AD, Jr., Nilsson L, Petrella RJ, Roux B, et al. CHARMM: the biomolecular simulation program. J Comput Chem. 2009;30:1545-614.
[40] Lee J, Cheng X, Swails JM, Yeom MS, Eastman PK, Lemkul JA, et al. CHARMM-GUI Input Generator for NAMD, GROMACS, AMBER, OpenMM, and CHARMM/OpenMM Simulations Using the CHARMM36 Additive Force Field. J Chem Theory Comput. 2016;12:405-13.
[41] Lee J, Hitzenberger M, Rieger M, Kern NR, Zacharias M, Im W. CHARMM-GUI supports the Amber force fields. J Chem Phys. 2020;153:035103.
[42] McGibbon RT, Beauchamp KA, Harrigan MP, Klein C, Swails JM, Hernandez CX, et al. MDTraj: A Modern Open Library for the Analysis of Molecular Dynamics Trajectories. Biophys J. 2015;109:1528-32.